

# MATTopo: Topology-preserving Medial Axis Transform with Restricted Power Diagram

NINGNA WANG, University of Texas at Dallas, USA

HUI HUANG, Shenzhen University, China

SHIBO SONG, Independent Researcher, China

BIN WANG, Tsinghua University, China

WENPING WANG, Texas A&M University, USA

XIAOHU GUO\*, University of Texas at Dallas, USA

We present a novel topology-preserving medial axis computation framework based on volumetric restricted power diagram (RPD), while preserving the medial features and geometric convergence simultaneously, for any input 3D CAD shape. The volumetric RPD discretizes the input 3D volume into sub-regions given a set of medial spheres. With this intermediate structure, we convert the homotopy equivalency between the generated medial mesh and the input 3D shape into a localized equivalency problem between each primitive of the medial mesh (vertex, edge, face) and its dual restricted elements (power cell, power face, power edge), by checking their connected components and Euler characteristics. We further propose a fractional Euler characteristic algorithm for efficient GPU-based computation of Euler characteristic for each restricted element on the fly while computing the volumetric RPD. Compared with existing voxel-based or sampling-based methods, our method is the first that can adaptively and directly revise the medial mesh without modifying the dependent structure globally, such as voxel size or sampling density, while preserving its topology and medial features. Compared with the feature preservation method MATFP [Wang et al. 2022], our method offers geometrically comparable results with fewer number of spheres, while more robustly captures the topology of input 3D shape.

CCS Concepts: • **Computing methodologies** → **Shape analysis**.

Additional Key Words and Phrases: Medial Axis Transform, Topology Preservation, Feature Preservation, Restricted Power Diagram

## ACM Reference Format:

Ningna Wang, Hui Huang, Shibo Song, Bin Wang, Wenping Wang, and Xiaohu Guo. 2024. MATTopo: Topology-preserving Medial Axis Transform with Restricted Power Diagram. 1, 1 (March 2024), 10 pages. <https://doi.org/10.1145/nnnnnnn.nnnnnnn>

\*Corresponding author

Authors' addresses: Ningna Wang, University of Texas at Dallas, USA, [ningna.wang@utdallas.edu](mailto:ningna.wang@utdallas.edu); Hui Huang, Shenzhen University, China, [hhzhiyan@gmail.com](mailto:hhzhiyan@gmail.com); Shibo Song, Independent Researcher, China, [longmaythess@outlook.com](mailto:longmaythess@outlook.com); Bin Wang, Tsinghua University, China, [wangbins@tsinghua.edu.cn](mailto:wangbins@tsinghua.edu.cn); Wenping Wang, Texas A&M University, USA, [wenping@tamu.edu](mailto:wenping@tamu.edu); Xiaohu Guo, University of Texas at Dallas, USA, [xguo@utdallas.edu](mailto:xguo@utdallas.edu).

Permission to make digital or hard copies of all or part of this work for personal or classroom use is granted without fee provided that copies are not made or distributed for profit or commercial advantage and that copies bear this notice and the full citation on the first page. Copyrights for components of this work owned by others than ACM must be honored. Abstracting with credit is permitted. To copy otherwise, or republish, to post on servers or to redistribute to lists, requires prior specific permission and/or a fee. Request permissions from [permissions@acm.org](mailto:permissions@acm.org).

© 2024 Association for Computing Machinery.

XXXX-XXXX/2024/3-ART \$15.00

<https://doi.org/10.1145/nnnnnnn.nnnnnnn>

## 1 INTRODUCTION

As a fundamental geometric structure, the medial axis [Blum et al. 1967] captures the topological equivalence and geometric protrusions of the input shape. The medial axis  $\mathcal{M}$  of a shape  $\mathcal{S}$  is defined as the set of vertices with two or more nearest neighbors on the shape boundary  $\partial\mathcal{S}$ . The *medial axis transform* (MAT) is a combination of the medial axis and its radius function. The topological and geometric properties of medial axis allow it to become the foundation for other skeletal shape descriptors [Tagliasacchi et al. 2016] and has been used in approximating [Ge et al. 2023; Hu et al. 2022, 2023; Lan et al. 2020; Yang et al. 2018, 2020], simplifying [Dou et al. 2022; Li et al. 2015; Yan et al. 2016], and analyzing shapes [Dou et al. 2020; Fu et al. 2022; Hu et al. 2019; Lin et al. 2021].

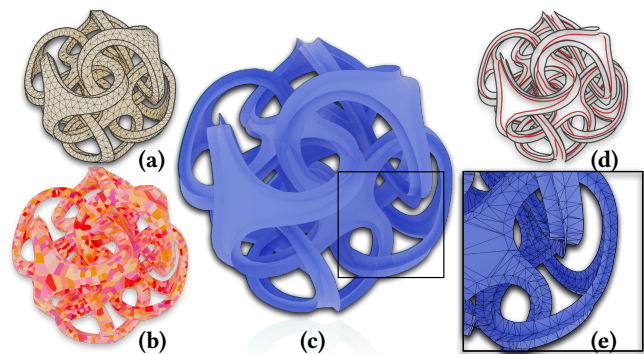


Fig. 1. We propose a novel volumetric RPD based framework for computing medial axis with preservation of topology, medial features, and geometry. (a) Input tetrahedral mesh with surface sharp features pre-detected; (b) the RPD of (c) the generated medial mesh; (d) the generated external (in black) and internal (in red) features; (e) the generated medial mesh zoomed-in.

One of the key property of MAT is its homotopy equivalence w.r.t. the given shape, *i.e.*, sharing the same set of connected components, holes and tunnels. *Euler characteristic* is the most commonly used topological indicator for measuring the topological property of a shape. For example, the Euler characteristic for a 3D volumetric torus shape is 0 and its corresponding MAT shares the same number. This number, however, serves as a global topological indicator, precluding us from identifying any problematic regions where the topological equivalence is ill-posed. The Voxel Cores (VC) method [Yan et al. 2018] can approximate the medial axes of any smooth shape with homotopy equivalence. However, it performs poorly when it

comes to geometric convergent approximation of any CAD models with non-smooth external features. Recent progress for computing MAT has shown privileges in preserving *medial features* as well as geometric convergence for CAD models using the surface restricted power diagram (RPD) based framework [Wang et al. 2022]. It cannot, however, guarantee the topological preservation for its generated medial mesh w.r.t. to the input model, as their experiments show inconsistency of the Euler characteristics.

In this paper, we present a novel framework for computing a topology-preserving MAT that is homotopy-equivalent to the input model. Our frameworks can also preserve both the external and internal medial features and ensure the geometric approximation accuracy. We have found that the volumetric RPD serves as a simple but effective intermediate structure between the input volumetric shape and the generated medial mesh. This structure allows us to localize the topological inconsistencies between the restricted power cells and its dual mesh. Owing to recent progress of GPU-based 3D power diagram computations [Basselin et al. 2021; Liu et al. 2020; Ray et al. 2018], we propose a volumetric RPD based strategy for topological checking and fixing that amends the medial mesh in a local manner, and propose a novel *fractional Euler characteristic* strategy for efficient GPU-based computation of the Euler characteristic of each restricted element (such as cells, faces, edges) on the fly while the volumetric RPD is computed. The initial medial mesh is generated using a small number of spheres (e.g., 50 spheres), then revised iteratively by adding new spheres in local regions and updating the corresponding partial RPD. Each revision only happens locally by checking individual restricted power cells (Sec. 4.1), their relations with neighboring power cells (Sec. 4.2), and their approximation to the input surface boundary (Sec. 4.3). Compared to existing sampling-based methods [Amenta et al. 2001; Miklos et al. 2010], voxel-based methods [Yan et al. 2018], and surface-RPD based method [Wang et al. 2022], our adaptive strategy can approximate the medial axes of any 3D CAD shapes with the preservation of homotopy equivalence, medial features, and geometric convergence, with a lower number of medial spheres required.

The main contributions of this paper include:

- We present a complete volumetric RPD based framework for computing 3D medial mesh of any CAD model with the preservation of homotopy equivalence, medial features, and geometric convergence.
- We propose an adaptive partial-RPD updating strategy for topological checking and fixing through the localized assessment of connected components and Euler characteristics for those restricted elements.
- We propose a novel fractional Euler characteristic algorithm for the efficient GPU-based computation of Euler characteristic for each restricted cell, face, and edge on the fly while computing the volumetric RPD parallelly.
- We propose an adaptive error-bounded strategy for computing medial axes of 3D shapes with geometric convergence.

## 2 RELATED WORKS

In this section, we review several representative works for approximating medial axis. Since our work relies on the computation of

power diagrams in restricted domains, we also review algorithms for computing restricted Voronoi and power diagrams in volumes.

### 2.1 Medial Axis Computation

The computation of medial axis mainly fall into the following three categories. Please refer to those survey materials [Siddiqi and Pizer 2008; Tagliasacchi et al. 2016] for more discussion.

*Algebraic methods* tend to create exact and analytic representation of MAT from a given boundary representation while tracing the features of medial axes (e.g., seam and junction) [Culver et al. 2004; Milenkovic 1993; Sherbrooke et al. 1996]. These methods, however, are algorithmically challenging and computationally expensive due to the need for solving non-linear systems, which limits the input of these methods to a simple class of shapes (e.g., polyhedron meshes with at most hundreds of faces).

*Voxel-based methods* attempt to approximate the medial axis by identifying a subset of the voxels which share the similar properties as medial axis [Saha et al. 2016; Sobiecki et al. 2014; Yan et al. 2018]. These methods, however, requires fine voxel resolution globally in order to meet both the topology and proximity guarantee, where the guidance of local adaptation is missing.

*Sampling-based methods* consider an interior subset of Voronoi diagram of surface samples placed on or around the shape's boundary. *Angle-based filtering methods* [Amenta et al. 2001; Brandt and Algazi 1992; Dey and Zhao 2002, 2004] are approaches to filter the Voronoi diagram and select the subset of Voronoi diagram of boundary sample satisfying an angle criteria.  *$\lambda$ -medial axis methods* [Chazal and Lieutier 2005; Pizer et al. 2003] discard a medial sphere if its radius is smaller than a given filtering threshold  $\lambda$ . These methods either struggle to preserve the topology of the input shape, or requires dense surface sampling to achieve the geometrical and topological convergence. The state-of-the-art method MATFP [Wang et al. 2022] uses the inner Voronoi vertices as initial sphere centers, then update those spheres' centers and radii as close as possible to the ground truth (GT), through a energy optimization framework. To the best of our knowledge, it is the first that attempts to approximate medial axes with non-smooth regions, such as convex sharp edges and corners (so called *external features*), as well as seams and junctions (so called *internal features*). It has, unfortunately, no topological guarantee of the generated medial mesh w.r.t. the input 3D shape.

None of the above MAT approximation methods is equipped with the ability to sample medial spheres adaptively and locally, without increasing the global supporting structures (e.g., voxel resolutions or sampling densities). Comparing with these methods, our method approximates the medial axis adaptively with the preservation of topology and geometry, at the same time shows equally strong ability to preserve both external features and internal features of the medial axis.

### 2.2 Restricted Voronoi and Power Diagram in Volumes

Robust and accurate computation of 3D volumetric RPD is not a trivial task. The classical clipping algorithm [Yan et al. 2010] and industrial-quality libraries, such as CGAL [Fabri and Pion 2009] and Geogram [Lévy and Filbois 2015], are still overly time-consuming

to be used in tasks that require frequent iterative RPD computations. Fortunately, recent GPU-based approaches has shown strong ability to compute Voronoi and power diagrams on highly parallel architectures, where the geometry of each Voronoi or power cell can be evaluated independently [Basselin et al. 2021; Liu et al. 2020; Ray et al. 2018]. Basselin et al. [2021] proposed a method to directly evaluate the integrals over every restricted power cell without computing the combinatorial structure of power diagram explicitly. Since our work requires explicit structure of each power cell, we build upon the ‘Tet-Cell’ strategy proposed by Liu et al. [2020]. After discretizing the volume into a tetrahedral mesh [Hu et al. 2020], the intersection of a tetrahedron (*tet* for short) with a cell can be calculated in a parallel manner. This parallel GPU-based volumetric RPD implementation reduces the computational cost significantly, e.g., from 8s to 0.6s for a model with 10k tets and 10k cells.

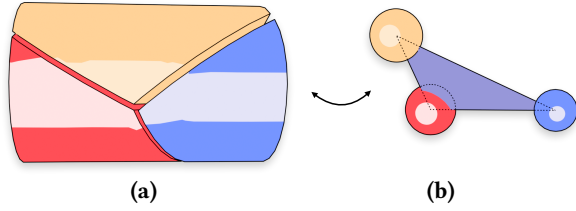


Fig. 2. The duality between the volumetric RPD (a) of three medial spheres and the generated medial mesh (b)

### 3 PRELIMINARIES

#### 3.1 Restricted Power Diagram and Medial Mesh

Similar to Voronoi diagram, the power diagram is generated by a set of weighted points, and coincide with the Voronoi diagram in the case of equal weights. A power diagram restricted within a bounded shape is called the *restricted power diagram* (RPD).

Following the convention in Q-MAT [Li et al. 2015], we approximate the MAT of a 3D shape using a non-manifold *medial mesh*  $\mathcal{M}_s$  consisting of triangles and edges. Each vertex of  $\mathcal{M}_s$  represents a *medial sphere*  $\mathbf{m} = (\theta, r)$ , with center  $\theta \in \mathbb{R}^3$  and radius  $r \in \mathbb{R}$ . Each edge  $\mathbf{e}_{ij}$  of  $\mathcal{M}_s$  is a linear interpolation of two spheres  $\mathbf{m}_i$  and  $\mathbf{m}_j$ . Similarly, each triangle face  $\mathbf{f}_{ijk}$  of  $\mathcal{M}_s$  is a linear interpolation of three spheres  $\mathbf{m}_i$ ,  $\mathbf{m}_j$ , and  $\mathbf{m}_k$ . The enveloping volume of edge and triangle of  $\mathcal{M}_s$  is called a *medial cone* and a *medial slab*, respectively.

MATFP [Wang et al. 2022] utilizes the duality of surface RPD to generate a medial mesh. However, it fails to preserve the homotopy equivalence of medial mesh w.r.t the input 3D shape. To overcome this deficiency, we construct the medial mesh directly from the duality of volumetric RPD. Fig. 2 (a) shows the RPD of three spheres, where the input volume is divided into three sub-domains clipped by three radical hyperplanes. We show its duality in Fig. 2 (b).

- Each sub-domain  $\omega(\mathbf{m}_i)$  is called a *restricted power cell* (RPC) of medial sphere  $\mathbf{m}_i$ , which is dual to a vertex on  $\mathcal{M}_s$ .
- The face shared by two adjacent RPCs is called a *restricted power face* (RPF),  $\omega_f(\mathbf{m}_i, \mathbf{m}_j)$ , which is dual to an edge  $\mathbf{e}_{ij}$  on  $\mathcal{M}_s$ .
- The edge shared by three RPCs is called a *restricted power edge* (RPE),  $\omega_e(\mathbf{m}_i, \mathbf{m}_j, \mathbf{m}_k)$ , which is dual to a triangle face  $\mathbf{f}_{ijk}$  on  $\mathcal{M}_s$ .

- A vertex shared by four RPCs  $\omega_v(\mathbf{m}_i, \mathbf{m}_j, \mathbf{m}_k, \mathbf{m}_s)$  is dual to a tet on  $\mathcal{M}_s$ , if it exists. Note that all tetrahedra in the medial mesh will be pruned with a thinning process similar to MATFP [Wang et al. 2022].

#### 3.2 Medial Sphere Generation

We follow the sphere classification method proposed in MATFP [Wang et al. 2022] to classify medial spheres. We use the following two medial sphere generation strategies for computing medial spheres that are tangent to at least two surface points. It is worth noting that medial spheres generated using these two methods are nearly ground truth spheres.

- *Sphere-shrinking* algorithm [Ma et al. 2012] for computing  $T_2$  medial spheres that are on **sheets** of the medial structure, and tangent to two different places on the surface;
- *Sphere-optimization* algorithm [Wang et al. 2022] for computing  $T_N$  ( $N \geq 3$ ) medial spheres that are on **seams** or **junctions** of the medial structure, and tangent to at least three different places on the surface.

#### 3.3 Restricted Power Cells (RPC) Computation

A power cell is a convex polyhedron that can be seen as an intersection of half-spaces, just like a Voronoi cell. The only difference is that these half-spaces are not generated by bisectors, but by radical hyperplanes.

We use the data structure introduced by Ray et al. [2018] to represent the convex polyhedrons, which is highly compact and well-suited for GPU implementation. Each half-space of the polyhedron is represented by a float4 storing 4 coefficients ( $a, b, c, d$ ) of plane equation  $ax + by + cz + d > 0$ . Each vertex of the polyhedron is the intersection of three half-spaces, therefore, is represented by a triplet of integers in a clockwise order, storing indices of three adjacent half-spaces.

To restrict the power cells in an input domain, we extend the ‘Tet-Cell’ strategy proposed by Liu et al. [2020]. After discretizing the input volumetric domain into a tetrahedral mesh [Hu et al. 2020], we compute the intersection between tetrahedral mesh and power cells. Each step discussed in Sec. 4 will adaptively insert new medial spheres when topological or geometrical deficiency is detected. We thus only update the RPD partially with cells relating to the newly added medial spheres, instead of re-computing the whole RPD. Please refer to our implementation details in the Supplementary Document for further discussions.

### 4 METHOD

Given a manifold tetrahedral mesh with its surface features (sharp edges and corners) pre-detected, our pipeline starts with an initial medial mesh of a small number (e.g., 50) of randomly placed medial spheres computed with the *sphere-shrinking* (Sec 3.2) algorithm [Ma et al. 2012]. The medial mesh is then refined iteratively through the following three steps. First, we preserve the homotopy equivalence of the generated medial mesh w.r.t the input 3D shape by examining two topological equivalence of all restricted elements for each medial sphere (Sec 4.1), as shown in Fig 3 (b). Then, the *medial*

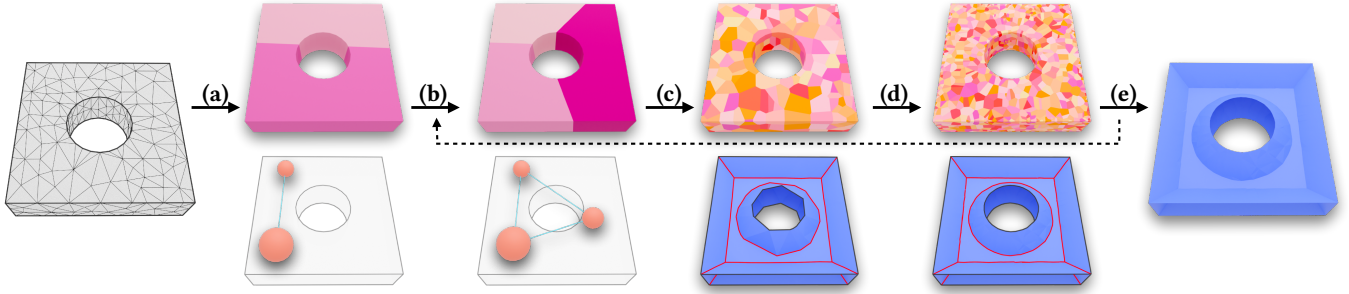


Fig. 3. The overview of our computational pipeline. Given a tetrahedral mesh with surface features (sharp edges and corners) pre-detected as input, our method starts with an initial medial mesh of a small number of spheres (*i.e.*, 2 spheres) using the *sphere-shrinking* algorithm [Ma et al. 2012], shown in (a). Then the homotopy equivalence of the generated medial mesh w.r.t. the input shape is preserved by examining the topological equivalence of individual RPCs (Sec 4.1), shown in (b). We preserve the *medial features* using the same method as MATFP [Wang et al. 2022] (Sec 4.2), shown in (c). Finally we preserve the geometric convergence based on a user-defined error threshold  $\delta^e$  (Sec 4.3), shown in (d). We repeat this process until both topological preservation and geometric convergence are satisfied, and output the final result of generated medial mesh, shown in (e).

features are preserved by assessing if the RPCs of two adjacent medial spheres covers the same surface regions (Sec. 4.2), as shown in Fig 3 (c). Finally, we ensure the geometric convergence by checking if the distance error between the shape boundary  $\partial S$  and the enveloping volume of medial mesh  $M_s$  is smaller than a user-defined threshold  $\delta^e$  (Sec. 4.3), as shown in Fig 3 (d). Each examination step is performed locally and new medial spheres are inserted for each preservation using two sphere generation strategies described in Sec. 3.2. For each iteration, we only update the RPD partially for cells that are related to the newly added medial spheres, rather than re-computing the whole RPD for all medial spheres. Please refer to the Supplementary Document for more implementation details.

#### 4.1 Topology Preservation

Given an input 3D volumetric shape, it is easy to calculate its topological measures in a global manner, *i.e.*, computing its *Euler characteristic* and the number of connected components. These indicators, however, are not helpful when it comes to tracing the ill-posed regions where the topological equivalence fails. In this paper, we utilize the volumetric RPD as a facilitator to ensure the topology equivalence between the input shape and the generated medial mesh. The global homotopy equivalence could be preserved as long as the equivalence between every local element of the volumetric RPD and its dual medial mesh is maintained.

The RPD of medial spheres  $\{\mathbf{m}_i\}_{i=1}^N$  decomposes the input volumetric domain  $S$  into a union of RPCs  $\{\omega_i\}_{i=1}^N$ . However, we extract its dual mesh as the medial mesh, which may not be homotopy-equivalent to the volumetric RPD (see Sec 3.1). Take Fig 4 (a) as an example, when we use a single medial sphere  $\mathbf{m}_1$  to represent the shape, its RPC is the whole torus that does not have the same topology as the medial sphere.

In light of the duality between each primitive of the medial mesh (vertex, edge, face) and each restricted element of the volumetric RPD (RPC, RPF, RPE) described in Sec 3.1, we can guarantee the homotopy equivalence between the original 3D shape and the generated medial mesh by enforcing the local topological equivalency between each primitive of the medial mesh and its corresponding

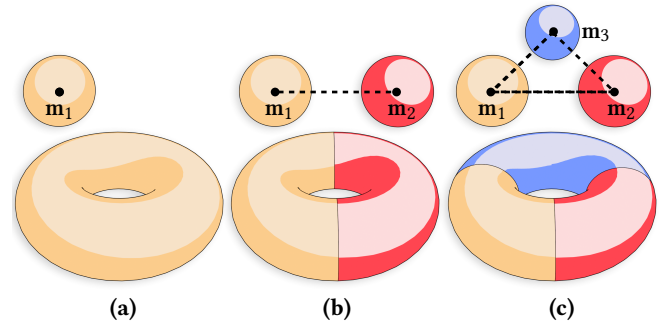


Fig. 4. The duality between the medial mesh (top) and volumetric RPD (bottom) for a 3D shape of torus, where the homotopy equivalence does not hold for case (a) and case (b). An additional medial sphere  $\mathbf{m}_3$  needs to be inserted in order to maintain the homotopy equivalence as shown in (c). We show the dual edges as black dotted lines.

dual restricted element in the RPD, *i.e.*, the equivalency between: vertex vs. RPC, edge vs. RPF, and face vs. RPE. Since the topology of each vertex, edge, and face is already known, we can simply perform the topology checking of each individual RPC and its associated RPFs and RPEs, by examining these two topological indicators:

- The number of *connected components* (CC number) tells us the maximal subset of a topological space;
- The *Euler characteristic* describes a topological space's structure regardless of the way it is bent. It can be calculated using following formula:  $Euler = V - E + F - C$ , where  $V$  is the number of vertices,  $E$  is the number of edges,  $F$  is the number of faces, and  $C$  is the number of volumetric cells.

To ensure homotopy equivalence, we are expecting each restricted element (*i.e.*, RPC, RPF, RPE) to have  $CC = 1$  and  $Euler = 1$ . For the example of Fig. 4 (a), the RPC of medial sphere  $\omega(\mathbf{m}_1)$  is the whole yellow torus, which has  $CC = 1$  but  $Euler = 0$ . The RPC  $\omega(\mathbf{m}_1)$  in Fig. 4 (b) has  $CC = 1$  and  $Euler = 1$  as expected, but its associated RPF  $\omega_f(\mathbf{m}_1, \mathbf{m}_2)$  has  $CC = 2$ . In Fig. 4 (c) all restricted elements have  $CC = 1$  and  $Euler = 1$  for all three medial spheres  $\mathbf{m}_1$ ,  $\mathbf{m}_2$  and  $\mathbf{m}_3$ . Note that only RPCs and RPFs exist in this example (c)



without any RPEs, hence only vertices and edges exist in the dual medial mesh. For each medial sphere  $\mathbf{m}_i$ , we perform a localized topological check for its corresponding restricted elements, and apply a straightforward refinement by adding new medial spheres if either their  $CC \neq 1$  or  $Euler \neq 1$ . The details of our preservation strategy for those two topological indicators are given in Sec. 4.1.1 and Sec. 4.1.2.

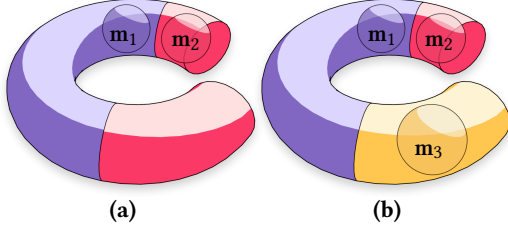


Fig. 5. Illustration of solving the CC number inequivalence described in Sec 4.1.1. The RPC of medial sphere  $\mathbf{m}_2$  in (a) contains two connected components, which is not topological consistent with its duality. Hence we add a new sphere  $\mathbf{m}_3$  to the other connected component of the RPC of  $\mathbf{m}_2$  for maintaining this equivalence.

**4.1.1 CC Number.** For a medial sphere  $\mathbf{m}_i$  and its corresponding restricted elements  $\omega(\mathbf{m}_i)$ ,  $\omega_f(\mathbf{m}_i, \mathbf{m}_j)$  and  $\omega_e(\mathbf{m}_i, \mathbf{m}_j, \mathbf{m}_k)$ , where  $\mathbf{m}_j$  and  $\mathbf{m}_k$  are the neighboring medial spheres of  $\mathbf{m}_i$ , we can trace their CC numbers using a simple traversal algorithm effortlessly. Once  $CC > 1$ , we add a new medial sphere to the connected component other than the one of the current medial sphere  $\mathbf{m}_i$ . In Fig. 4 (b), the RPF  $\omega_f(\mathbf{m}_1, \mathbf{m}_2)$  has  $CC = 2$ , while in Fig. 5 (a), the RPC  $\omega(\mathbf{m}_2)$  has  $CC = 2$ . To fix these issues, we randomly choose a surface point on one of the CC of the RPF, or choose a surface point on the other CC of the RPC (other than where the medial sphere resides), and use it as the *pin point* for the *sphere-shrinking* algorithm (see Sec. 3) to add a new medial sphere  $\mathbf{m}_3$ , as shown in Fig. 4 (c) and Fig 5 (b).

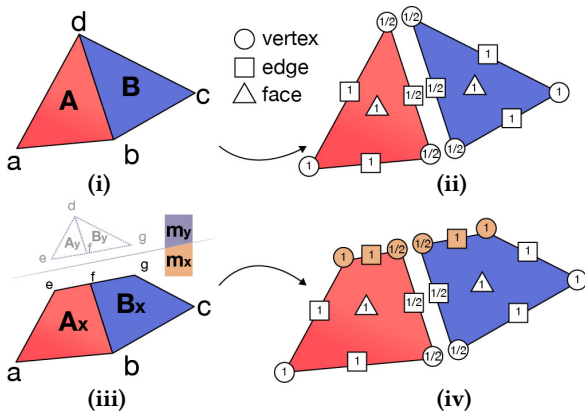


Fig. 6. 2D illustration of our GPU-based Euler characteristic computation on-the-fly during the clipping process of RPD. The number shown in each vertex, edge, and face represents its *Fractional Euler Characteristic*, as described in Sec 4.1.2.

**4.1.2 Euler Characteristic.** One can compute the Euler characteristic of each restricted element (RPC, RPF and RPE) after obtaining the explicit RPD representation through the clipping process. However, current GPU-based implementations either directly evaluate integrals over every cells without computing the combinatorial data structure of power diagram [Basselin et al. 2021], or store the dual form of cells using a simple triangle mesh [Liu et al. 2020; Ray et al. 2018] but requires costly post-processing steps to access the exact combinatorial data structure of the cells. This is due to the fact that these methods are well-designed for the high parallelism of GPU, and are optimized for applications that only requires integrals over the cells, e.g., fluid dynamics simulations. Therefore, in this paper we propose a *Fractional Euler Characteristic* strategy to collect Euler characteristics on-the-fly, by taking full advantage of the existing GPU-based volumetric RPD computation pipeline.

Similar to the *Tet-Cell* strategy proposed by Liu et al. [2020], our pipeline take the tetrahedral mesh as input, where the Euler characteristic is inherited during the clipping process. For each tet of related medial sphere  $\mathbf{m}_i$ , we clip the RPC  $\omega(\mathbf{m}_i)$  as the intersection of half-spaces bounded by the bisectors of  $\mathbf{m}_i$  and its power neighbors [Ray et al. 2018]. The implementation details of finding tet-sphere relations and sphere neighbors are given in the Supplementary Document.

**Fractional Euler Characteristics.** Fig. 6 shows a 2D illustration of our proposed *fractional Euler characteristics*, and how these fractional numbers are inherited during the clipping process of RPD computation. In this example, the target Euler characteristic is 1 for the 2D shape, i.e., 4 (vertices) - 5 (edges) + 2 (faces) - 0 (cells) = 1. It contains 2 triangles A and B in Fig. 6 (i), and the fractional Euler characteristic of each element is shown in Fig. 6 (ii). Note that both vertex b or d are shared between A and B, so their fractional Euler characteristic inside each triangle is only  $\frac{1}{2}$ . The same reason for the fractional Euler characteristic  $\frac{1}{2}$  for the edge (b, d) inside each triangle. As an initialization to our GPU-based tet-cell clipping, whenever a tetrahedral mesh is inputted to GPU, such fractional Euler characteristics are inputted together with the mesh, based on the combinatorial structure of the tetrahedral mesh.

**Inheritance of Fractional Euler Characteristics during RPD Clipping.** During the parallel execution of clipping process [Ray et al. 2018], the half-space  $\Pi^+(\mathbf{m}_x, \mathbf{m}_y)$  of two medial spheres  $\mathbf{m}_x$  and  $\mathbf{m}_y$  cuts each triangle into two parts, thus new vertices and edges emerge. The fractional Euler characteristics of new vertices are inherited from their pre-clipped edges, and those of the new edges are inherited from its pre-clipped faces. For the example of Fig. 6, the new vertex f inherits the fractional Euler characteristic  $\frac{1}{2}$  from its pre-clipped edge (b, d), and the new edge (e, f) inherits the fractional Euler characteristic 1 from its pre-clipped face A. Note that during the clipping process, although the new generated vertices, edges, and faces could be shared between different cells, we no longer divide their fractional Euler characteristics. For example, in Fig. 6 (iii), although the new edge (e, f) is shared between two cells  $A_x$  and  $A_y$ , we only set its fractional Euler characteristic as 1 for cell  $A_x$ , and 1 for cell  $A_y$ . This is because the use of fractional Euler characteristics is to facilitate the easy counting of Euler characteristic of each restricted power element associated with a particular

sphere. For the example of Fig. 6 (iv), we are only interested in the Euler characteristics for the restricted elements related to sphere  $\mathbf{m}_x$ , thus the fractional Euler characteristics of those newly generated vertices and edges will not be shared with the other spheres.

Through such inheritance, the fractional Euler characteristic of all restricted elements (RPCs, RPFs, RPEs) for sphere  $\mathbf{m}_x$  can be obtained on-the-fly during the parallel clipping process. In Fig. 6 (iv), the final RPFs of sphere  $\mathbf{m}_x$  consists of two convex hulls  $\mathbf{A}_x$  and  $\mathbf{B}_x$ , and its Euler characteristic can be computed by  $Euler(\mathbf{A}_x) + Euler(\mathbf{B}_x) = 1$ , where:

$$\begin{aligned} Euler(\mathbf{A}_x) &= (1 + 1 + \frac{1}{2} + \frac{1}{2}) - (1 + 1 + 1 + \frac{1}{2}) + (1) = \frac{1}{2}, \\ Euler(\mathbf{B}_x) &= (1 + 1 + \frac{1}{2} + \frac{1}{2}) - (1 + 1 + 1 + \frac{1}{2}) + (1) = \frac{1}{2}. \end{aligned} \quad (1)$$

For each medial sphere, we collect the fractional Euler characteristics for all of its restricted elements (RPCs, RPFs, RPEs) during the runtime of clipping process, then check if the target Euler characteristic for each element is expected or not, e.g., in Fig. 4 (a), the sphere  $\mathbf{m}_1$  has its RPC  $\omega(\mathbf{m}_1)$  with  $Euler(\omega(\mathbf{m}_1)) = 0$ . To fix this issue, we search all the surface triangles among the RPC of sphere  $\mathbf{m}_1$  and target the furthest one as the *pin point* and uses the *sphere-shrinking* algorithm (see Sec. 3) to add a new sphere  $\mathbf{m}_2$ . After that, the RPF between  $\mathbf{m}_1$  and  $\mathbf{m}_2$  has  $CC = 2$ , which will trigger the insertion of a new sphere  $\mathbf{m}_3$ , with the same process described in Sec. 4.1.1.

## 4.2 Medial Feature Preservation

*External features*, such as convex sharp edges and corners, are commonly seen in CAD models and are pre-detected as input for our algorithm. We adopt the similar feature preservation strategies as MATFP [Wang et al. 2022]. Unlike MATFP which starts with a dense number of initial spheres, our method begins with a smaller set of non-feature medial spheres (e.g., 50 spheres). Hence, instead of removing redundant non-feature spheres that ‘invade’ the RPCs of two neighboring feature spheres on a sharp edge, we examine the individual RPC and add new zero-radius feature spheres iteratively if any sharp edge belongs to the cell of a non-feature sphere. As a result, all convex sharp edges reside in cells corresponding to some zero-radius feature spheres, which preserves the convex sharp edges in generated medial mesh as dual of volumetric RPD. For corners and concave sharp features, we follow the same medial feature preservation strategies as MATFP.

*Internal features* are preserved by inserting new internal feature spheres after detecting the deficiency, similar to MATFP [Wang et al. 2022]. Here we maintain a queue of all medial edges in the medial mesh with random order, and check whether two connected medial spheres of each edge belong to the same medial sheets as they touch the same surface regions using the surface part of their RPCs.

## 4.3 Geometry Preservation

The medial mesh generated through above steps is topologically correct and captures medial features, however, its reconstruction may not geometrically converge to the input shape, since we adaptively insert spheres from a low number. We propose an error-bounding strategy so that the geometric error from the input shape to the reconstructed mesh is bounded by a user-controlled threshold  $\delta^\epsilon$ .

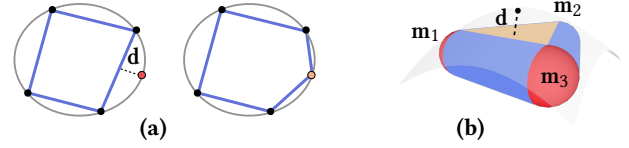


Fig. 7. Illustration of geometric preservation. (a) We compute the distance  $d$  from the sampled points (in red) on external features to the nearest feature enveloping cone and add zero-radius medial sphere (in yellow) if the distance is too large. For other cases (b), we randomly sample surface points and compute their distance to the nearest enveloping primitive of the medial mesh, and insert a new non-feature sphere if the distance is too large.

For preserving the geometry of external features, we sample points directly on those pre-detected features, such as Fig 7 (a) in red, and compute their distance  $d$  to the nearest enveloping cone. When the distance is larger than our threshold, which often happens for curved feature lines, we insert a new zero-radius feature sphere (Fig 7 (a) in yellow). For other cases, we use the distance from any surface sample to the closest enveloping element as the metric, see Fig 7 (b). For each surface sample, we compute its distance to the closest enveloping volume of the medial mesh (sphere, cone, slab described in Sec 3.1) in GPU. If the ratio of the distance  $d$  over the diagonal of bounding box is larger than a user-defined threshold  $\delta^\epsilon$ , we insert a new non-feature sphere with the surface sample as the pin point using the *sphere-shrinking* algorithm [Ma et al. 2012]. As more non-feature spheres are inserted, the enveloping volume of the medial mesh is converging to the input shape geometrically. We show an ablation study on the impact of the value of  $\delta^\epsilon$  in Sec 5.3.

## 5 EXPERIMENTS

In this section, we show quantitative and qualitative evaluations of the proposed method. We implemented our algorithm in C++ and CUDA, using Geogram [Lévy and Filbois 2015] for linear algebra routines. We ran our experiments on a computer with a 3.60GHz Intel(R) Core(TM) i7-9700K CPU, NVIDIA GeForce RTX 2080 Ti GPU, and 32 GB memory. We ran our method on the first 100 models in the ABC dataset [Koch et al. 2019] under the *10k/test* folder using 2048 as the number of mesh vertices, same as MATFP [Wang et al. 2022]. All model sizes are normalized to the  $[0, 1000]^3$  range. We use fTetwild [Hu et al. 2020] for computing the initial tetrahedral mesh from triangle mesh with parameters  $l = 0.5$ .

*Evaluation Metrics.* We use the *Euler characteristics*  $E$  as the topology measures for the generated medial mesh, and show the ground truth Euler characteristic of the input shape as ‘GT Euler’. We use the two-sided Hausdorff distance error  $\epsilon$  to measure the the surface reconstruction accuracy using the generated medial meshes.  $\epsilon^1$  is the one-sided Hausdorff distance from the original surface to the surface reconstructed from MAT, and  $\epsilon^2$  is the distance in reverse side. All Hausdorff distances are evaluated as percentages of the distance over the diagonal lengths of the models’ bounding box. The  $\epsilon^{max}$  is the maximum of  $\epsilon^1$  and  $\epsilon^2$ . We show  $\#s$  as the number of medial spheres for the medial meshes generated from each method, and use  $\#t$  as the number of tets in the input tetrahedron mesh.

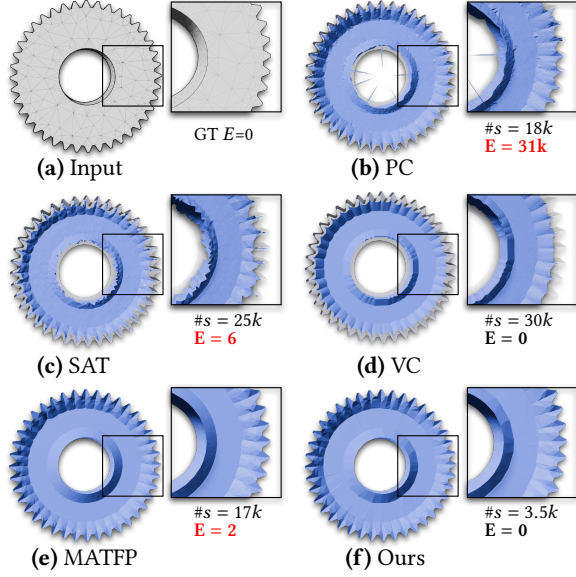


Fig. 8. Qualitative comparison of topology preservation between our method and MATFP [Wang et al. 2022], PC [Amenta et al. 2001], SAT [Miklos et al. 2010], and VC [Yan et al. 2018]. The ground truth *Euler characteristic* is shown in (a), and  $\#s$  represents the number of medial spheres generated.

### 5.1 Comparison with MATFP method

We compare our method with MATFP [Wang et al. 2022] regarding the topology preservation. To our best knowledge, MATFP is the state-of-the-art method for computing medial axis of CAD models, which preserves both external and internal features. However, it also has a clear drawback with no guarantee of topology preservation for the generated medial mesh w.r.t. the input model. The key advantage of our method is its ability in preserving the topology, while maintaining the ability to capture external and internal features. We show the Euler characteristic  $E$  in Table 1 for those models that the output of MATFP deviates from the GT *Euler*. Our method, on the contrary, can preserve the topology while keeping a competitive reconstruction quality.

Beside preserving topology, our method also generates almost 10 times less number of medial spheres  $\#s$  than MATFP in the final medial mesh, shown in Table 1 and Fig 8. MATFP favors preserving external feature or internal feature by adding as many feature spheres as possible during each step. This will inevitable result in a large number of medial spheres, mostly redundant, in the generated medial mesh. Owing to the proposed adaptive refinement strategy, our method can add only few (even single) number of new medial spheres at each iteration and update the RPD partially using GPU. Each updated partial RPD will change the medial mesh connectivity within the corresponding local regions, as dual of volumetric RPD. These newly added medial spheres may already satisfy the criteria for local structures, thus avoiding other similar spheres (i.e., spheres with similar centers and radii) to be inserted.

Since we use the same feature preservation strategy as MATFP, our methods shows comparable if not better reconstruction quality, as shown in Table 1 and Fig. 10. More visualizations are shown in Fig. 12. Specifically, we use  $\delta^\epsilon = 0.6$  for model showing in Fig 10.

Table 1. Quantitative comparison on topology preservation with MATFP [Wang et al. 2022].  $\#s$  is the number of generated medial spheres.  $\epsilon^{max}$  is the two-sided Hausdorff Distance between the original surface and reconstruction, as maximum of  $\epsilon^1$  and  $\epsilon^2$  described in Sec. 5. We show the Euler characteristic as  $E$  and ground truth as 'GT Euler'. Comparing to MATFP which has no guarantee of homotopy equivalence, our method gives correct Euler characteristic with lower number of generated medial spheres and competitive reconstruction quality.

Model ID (GT Euler)	#s	MATFP $\epsilon^{max}$	$E$	#s	Ours $\epsilon^{max}$	$E$
549 (-6)	21k	1.282	-5	7.2k*	<b>1.077</b>	-6
4123 (-3)	17k	3.799	-1	5.1k*	<b>1.095</b>	-3
5227 (-5)	12k	<b>0.442</b>	5	3.2k*	1.419	-5
8315 (-4)	11k	3.351	-2	1.5k*	<b>1.481</b>	-4
8964 (-72)	25k	<b>0.251</b>	-37	8.7k*	0.753	-72
10836 (-1)	3k	<b>1.067</b>	1	2.7k*	1.496	-1
11299 (-24)	19k	2.324	-13	5.8k*	<b>0.961</b>	-24
11790 (0)	17k	1.79	2	5.3k*	<b>0.819</b>	0
11835 (0)	21k	2.252	-16	5.4k*	<b>1.015</b>	0
13026 (-4)	26k	2.203	-2	10k*	<b>1.241</b>	-4
13607 (-13)	19k	<b>0.956</b>	-19	7.3k*	1.486	-13
14621 (-3)	34k	2.812	-9	12k*	<b>0.982</b>	-3
15094 (-8)	35k	<b>1.045</b>	-4	7.2k*	1.462	-8

For more detailed statistics, please refer to the Supplementary Document.

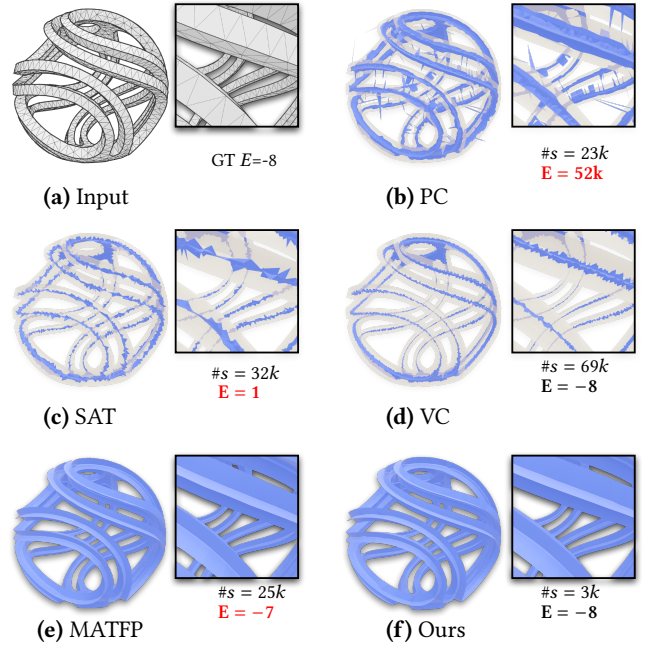


Fig. 9. Comparison of the medial feature preservation ability between our method and PC [Amenta et al. 2001], SAT [Miklos et al. 2010], VC [Yan et al. 2018], and MATFP [Wang et al. 2022]. Our method can not only preserve medial features, but also output the correct topology of the medial mesh.

### 5.2 Comparison with PC, SAT, and VC Methods

We compare our method with three classical methods for approximating medial axis, including two sampling-based methods – PC



(Power Crust [Amenta et al. 2001]) and SAT (Scaled Axis Transform [Miklos et al. 2010]), and one voxel-based method VC (Voxel Cores [Yan et al. 2018]), regarding feature and topology preservation quality (Fig 9), and surface reconstruction quality from the generated medial mesh (Fig 10).

We test the PC [Amenta et al. 2001] method using two different sampling densities, and experiment SAT [Miklos et al. 2010] method using two values of sampling parameter:  $\delta = 0.04$  and  $\delta = 0.03$  in Fig 10, and set the scale parameter as default 1.0 in all experiments. Similar to all other sampling-based methods, the quality of medial mesh generated would improve when the surface density increases. However, these two methods generate medial meshes that are not thin with large number of flat tetrahedrons, and Euler characteristic value varies as shown in Fig 8, *i.e.*,  $E = 31k$  and  $E = 6$  respectively. In addition, they cannot preserve any medial features, both externally and internally, as shown in Fig 9.

We also compare with VC [Yan et al. 2018] method regarding the reconstruction quality and the feature preservation quality of generated medial mesh. We use two voxel sizes  $2^8$  and  $2^9$  with pruning parameters  $\lambda = 0.03$ , shown in Fig 10. Even though VC can output the topologically-correct medial mesh, it requires large number of medial spheres for outputting a smooth structure around the internal features, almost 10 times more than our method (*i.e.*,  $30k$  in Fig 8). This is due to the fact that VC controls the sampling globally based on the size of the voxels. Smaller voxel size would generates denser medial spheres. It cannot, however, directly control the sampling rate of medial spheres as needed. We also found that the medial mesh generated from VC shrinks more as the value of pruning parameter increases, which will result in a more rounded reconstruction result around the external features.

### 5.3 Ablation Study on Geometric Error Bound $\delta^\epsilon$

One important parameter used in our method is the user-defined geometric error bound  $\delta^\epsilon$ , which controls the one-side reconstruction accuracy (from input surface to the reconstructed mesh). Here the error is measured by the distance from surface samples to the enveloping volume of the medial mesh. Similar to Hausdorff distance described in Sec 5, this error is also scaled based on the diagonal length of the shape's bounding box. We show the effect of two different values of the parameter  $\delta^\epsilon$  in Fig. 11.

A smaller value of  $\delta^\epsilon$  would generate a smoother medial mesh around non-feature regions, as more non-feature spheres are sampled. It can also reduce the non-smooth connections on medial features, either external or internal ones (see the black and red curves respectively in Fig. 11). As a result, a smaller error bound will inevitably output a reconstructed mesh with better quality.

## 6 LIMITATIONS AND FUTURE WORK

Our method can produce an approximated MAT that is visually and quantitatively similar to those of MATFP [Wang et al. 2022] geometry-wise, with less number of spheres and the additional benefit of topology preservation. However it comes with the cost of more computational time. Although both our method and MATFP rely on RPD, the former uses volumetric RPD which requires cutting tets by half-spaces inside the volume, while the latter uses surface

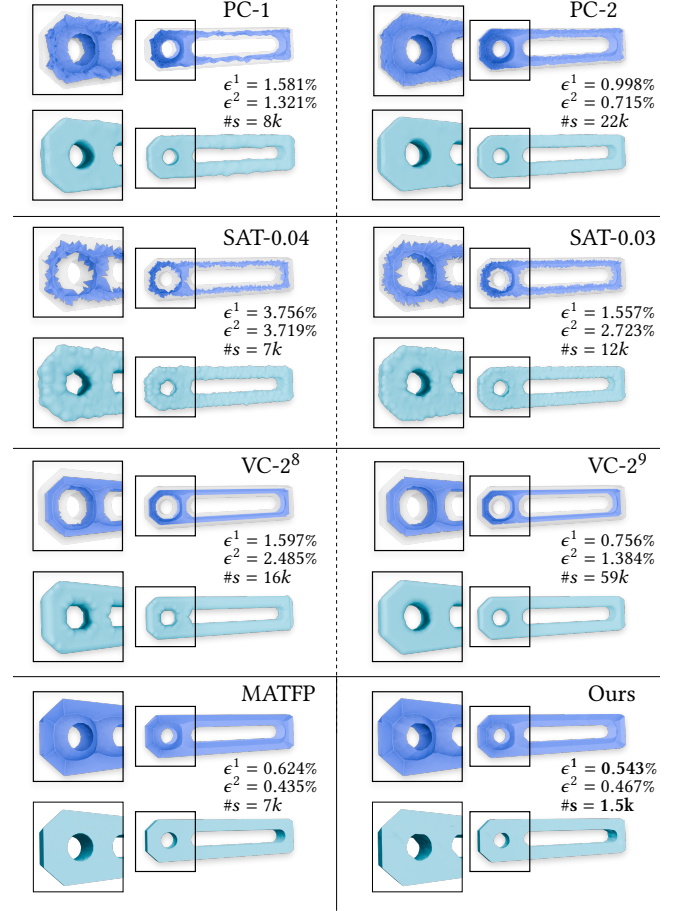


Fig. 10. Qualitative comparison of the medial mesh and the reconstructed mesh among ours and PC [Amenta et al. 2001], SAT [Miklos et al. 2010], VC [Yan et al. 2018], and MATFP [Wang et al. 2022]. Here  $\epsilon^1$  and  $\epsilon^2$  are the Hausdorff distance errors described in Sec 5.

Table 2. Statistic of our running time in seconds. #t is the number of tets in the given tetrahedron mesh. #s is the number of generated medial spheres. #RPD is the number of volumetric RPD calculated.  $S_{topo}$  is the running time of topology preservation step (Sec. 4.1).  $S_{extf}$  and  $S_{intf}$  is the running time for preserving external features and internal features (Sec 4.2). The model's ID# correspond to those shown in Table 1.

Model ID	#t	#s	#RPD	$S_{topo}$	$S_{extf}$	$S_{intf}$	$S_{geo}$	Total (s)
549	8k	7.2k	34	74	115	376	99	664
4123	1.2k	5.1k	35	15	42	109	32	198
5227	1k	5.1k	31	10	22	23	17	72
8315	4k	1.5k	37	64	73	444	112	693
8964	3.6k	8.7k	28	36	113	394	16	559
10836	3.8k	2.7k	41	30	29	126	63	248

RPD which only considers the intersection between triangle and half-spaces. As the runtime statistics shown in Table 2, our method takes minutes for each model even though each step's calculation of volumetric RPD on GPU only takes about 1-3 seconds. In the future, we will consider parallelising the feature preserving ( $S_{extf}$  and  $S_{intf}$ ) stage as much as possible to reduce the runtime.



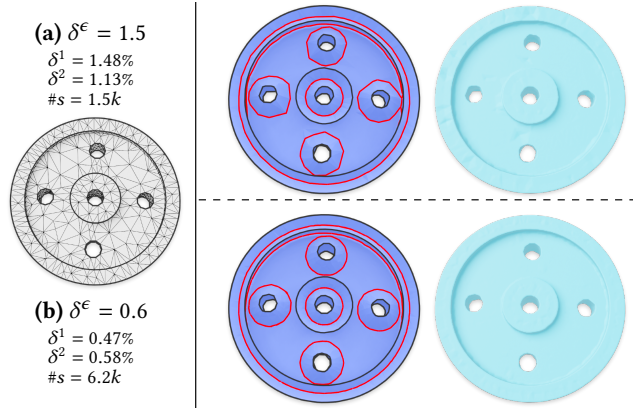


Fig. 11. Ablation study on geometric error bound  $\delta^\epsilon$ . We use two different error bounds: (a)  $\delta^\epsilon = 1.5$  and (b)  $\delta^\epsilon = 0.6$ . Smaller error bound can generate a medial mesh with smoother features which results in a better reconstruction quality.

Moreover, our current GPU-based implementation may fail to compute RPD if the given tetrahedral mesh has a very large number of tets. For example, the model #12280 in Supplementary Document contains over 5.5 million tets even using the fTetwild [Hu et al. 2020] with the largest length parameter value  $l = 1$ . We leave this computational issue for future exploration. We plan to publicize our source code and data online once the paper is accepted.

## REFERENCES

- Nina Amenta, Sunghee Choi, and Ravi Krishna Kolluri. 2001. The power crust. In *Proceedings of the sixth ACM symposium on Solid modeling and applications*. 249–266.
- Justine Basselin, Laurent Alonso, Nicolas Ray, Dmitry Sokolov, Sylvain Lefebvre, and Bruno Lévy. 2021. Restricted power diagrams on the GPU. In *Computer Graphics Forum*, Vol. 40. Wiley Online Library, 1–12.
- Harry Blum et al. 1967. *A transformation for extracting new descriptors of shape*. Vol. 43. MIT press Cambridge, MA.
- Jonathan W Brandt and V Ralph Algazi. 1992. Continuous skeleton computation by Voronoi diagram. *CVGIP: Image understanding* 55, 3 (1992), 329–338.
- Frédéric Chazal and André Lieutier. 2005. The “ $\lambda$ -medial axis”. *Graphical Models* 67, 4 (2005), 304–331.
- Tim Culver, John Keyser, and Dinesh Manocha. 2004. Exact computation of the medial axis of a polyhedron. *Computer Aided Geometric Design* 21, 1 (2004), 65–98.
- Tamal K Dey and Wulue Zhao. 2002. Approximate medial axis as a voronoi subcomplex. In *Proceedings of the seventh ACM symposium on Solid modeling and applications*. 356–366.
- Tamal K Dey and Wulue Zhao. 2004. Approximating the medial axis from the Voronoi diagram with a convergence guarantee. *Algorithmica* 38, 1 (2004), 179–200.
- Zhiyang Dou, Cheng Lin, Rui Xu, Lei Yang, Shiqing Xin, Taku Komura, and Wenping Wang. 2022. Coverage Axis: Inner Point Selection for 3D Shape Skeletonization. In *Computer Graphics Forum*, Vol. 41. Wiley Online Library, 419–432.
- Zhiyang Dou, Shiqing Xin, Rui Xu, Jian Xu, Yuanfeng Zhou, Shuangmin Chen, Wenping Wang, Xiuyang Zhao, and Changhe Tu. 2020. Top-down shape abstraction based on greedy pole selection. *IEEE Transactions on Visualization and Computer Graphics* 27, 10 (2020), 3982–3993.
- Andreas Fabri and Sylvain Pion. 2009. CGAL: The computational geometry algorithms library. In *Proceedings of the 17th ACM SIGSPATIAL international conference on advances in geographic information systems*. 538–539.
- Zhiying Fu, Rui Xu, Shiqing Xin, Shuangmin Chen, Changhe Tu, Chenglei Yang, and Lin Lu. 2022. Easyvrmodeling: Easily create 3d models by an immersive vr system. *Proceedings of the ACM on Computer Graphics and Interactive Techniques* 5, 1 (2022), 1–14.
- Mengyuan Ge, Junfeng Yao, Baorong Yang, Ningna Wang, Zhonggui Chen, and Xiaohu Guo. 2023. Point2MM: Learning medial mesh from point clouds. *Computers & Graphics* 115 (2023), 511–521.
- Jianwei Hu, Gang Chen, Baorong Yang, Ningna Wang, Xiaohu Guo, and Bin Wang. 2022. IMMAT: Mesh reconstruction from single view images by medial axis transform prediction. *Computer-Aided Design* 150 (2022), 103304.
- Jianwei Hu, Bin Wang, Lihui Qian, Yiling Pan, Xiaohu Guo, Lingjie Liu, and Wenping Wang. 2019. MAT-Net: Medial Axis Transform Network for 3D Object Recognition. In *Proceedings of the 28th International Joint Conference on Artificial Intelligence (IJCAI’19)*. 774–781.
- Jianwei Hu, Ningna Wang, Baorong Yang, Gang Chen, Xiaohu Guo, and Bin Wang. 2023. S3DS: Self-supervised Learning of 3D Skeletons from Single View Images. In *Proceedings of the 31st ACM International Conference on Multimedia*. 6948–6958.
- Yixin Hu, Tesse Schneider, Bolun Wang, Denis Zorin, and Daniele Panozzo. 2020. Fast tetrahedral meshing in the wild. *ACM Transactions on Graphics (TOG)* 39, 4 (2020), 117–1.
- Sebastian Koch, Albert Matveev, Zhongshi Jiang, Francis Williams, Alexey Artemov, Evgeny Burnaev, Marc Alexa, Denis Zorin, and Daniele Panozzo. 2019. Abc: A big cad model dataset for geometric deep learning. In *Proceedings of the IEEE/CVF conference on computer vision and pattern recognition*. 9601–9611.
- Lei Lan, Ran Luo, Marco Fratarcangeli, Weiwei Xu, Huamin Wang, Xiaohu Guo, Junfeng Yao, and Yin Yang. 2020. Medial Elastics: Efficient and Collision-Ready Deformation via Medial Axis Transform. *ACM Trans. Graph.* 39, 3, Article 20 (apr 2020).
- Bruno Lévy and Alain Filbois. 2015. Geogram: a library for geometric algorithms. (2015).
- Pan Li, Bin Wang, Feng Sun, Xiaohu Guo, Caiming Zhang, and Wenping Wang. 2015. Q-mat: Computing medial axis transform by quadratic error minimization. *ACM Transactions on Graphics (TOG)* 35, 1 (2015), 1–16.
- Cheng Lin, Changjian Li, Yuan Liu, Nenglu Chen, Yi-King Choi, and Wenping Wang. 2021. Point2skeleton: Learning skeletal representations from point clouds. In *Proceedings of the IEEE/CVF conference on computer vision and pattern recognition*. 4277–4286.
- Xiaohan Liu, Lei Ma, Jianwei Guo, and Dong-Ming Yan. 2020. Parallel computation of 3D clipped Voronoi diagrams. *IEEE Transactions on Visualization and Computer Graphics* 28, 2 (2020), 1363–1372.
- Jaehwan Ma, Sang Won Bae, and Sunghee Choi. 2012. 3D medial axis point approximation using nearest neighbors and the normal field. *The Visual Computer* 28, 1 (2012), 7–19.
- Balint Miklos, Joachim Giesen, and Mark Pauly. 2010. Discrete scale axis representations for 3D geometry. In *ACM SIGGRAPH 2010 papers*. 1–10.
- Victor Milenkovic. 1993. Robust Construction of the Voronoi Diagram of a Polyhedron.. In *CCCC*, Vol. 93. Citeseer, 473–478.
- Stephen M Pizer, Kaleem Siddiqi, Gabor Székely, James N Damon, and Steven W Zucker. 2003. Multiscale medial loci and their properties. *International Journal of Computer Vision* 55, 2 (2003), 155–179.
- Nicolas Ray, Dmitry Sokolov, Sylvain Lefebvre, and Bruno Lévy. 2018. Meshless Voronoi on the GPU. *ACM Transactions on Graphics (TOG)* 37, 6 (2018), 1–12.
- Punam K Saha, Gunilla Borgefors, and Gabriella Sanniti di Baja. 2016. A survey on skeletonization algorithms and their applications. *Pattern recognition letters* 76 (2016), 3–12.
- Evan C Sherbrooke, Nicholas M Patrikalakis, and Erik Brisson. 1996. An algorithm for the medial axis transform of 3D polyhedral solids. *IEEE transactions on visualization and computer graphics* 2, 1 (1996), 44–61.
- Kaleem Siddiqi and Stephen Pizer. 2008. *Medial representations: mathematics, algorithms and applications*. Vol. 37. Springer Science & Business Media.
- André Sobiecki, Andrei Jalba, and Alexandru Telea. 2014. Comparison of curve and surface skeletonization methods for voxel shapes. *Pattern Recognition Letters* 47 (2014), 147–156.
- Andrea Tagliasacchi, Thomas Delame, Michela Spagnuolo, Nina Amenta, and Alexandru Telea. 2016. 3d skeletons: A state-of-the-art report. In *Computer Graphics Forum*, Vol. 35. Wiley Online Library, 573–597.
- Ningna Wang, Bin Wang, Wenping Wang, and Xiaohu Guo. 2022. Computing Medial Axis Transform with Feature Preservation via Restricted Power Diagram. *ACM Transactions on Graphics (Proceedings of SIGGRAPH Asia 2022)* 41, 6 (2022).
- Dong-Ming Yan, Wenping Wang, Bruno Lévy, and Yang Liu. 2010. Efficient computation of 3D clipped Voronoi diagram. In *Advances in Geometric Modeling and Processing: 6th International Conference, GMP 2010, Castro Urdiales, Spain, June 16–18, 2010. Proceedings* 6. Springer, 269–282.
- Yajie Yan, David Letscher, and Tao Ju. 2018. Voxel cores: Efficient, robust, and provably good approximation of 3d medial axes. *ACM Transactions on Graphics (TOG)* 37, 4 (2018), 1–13.
- Yajie Yan, Kyle Sykes, Erin Chambers, David Letscher, and Tao Ju. 2016. Erosion thickness on medial axes of 3D shapes. *ACM Transactions on Graphics (TOG)* 35, 4 (2016), 1–12.
- Baorong Yang, Junfeng Yao, and Xiaohu Guo. 2018. DMAT: Deformable medial axis transform for animated mesh approximation. In *Computer Graphics Forum*, Vol. 37. Wiley Online Library, 301–311.
- Baorong Yang, Junfeng Yao, Bin Wang, Jianwei Hu, Yiling Pan, Tianxiang Pan, Wenping Wang, and Xiaohu Guo. 2020. P2MAT-NET: Learning medial axis transform from sparse point clouds. *Computer Aided Geometric Design* 80 (2020), 101874.

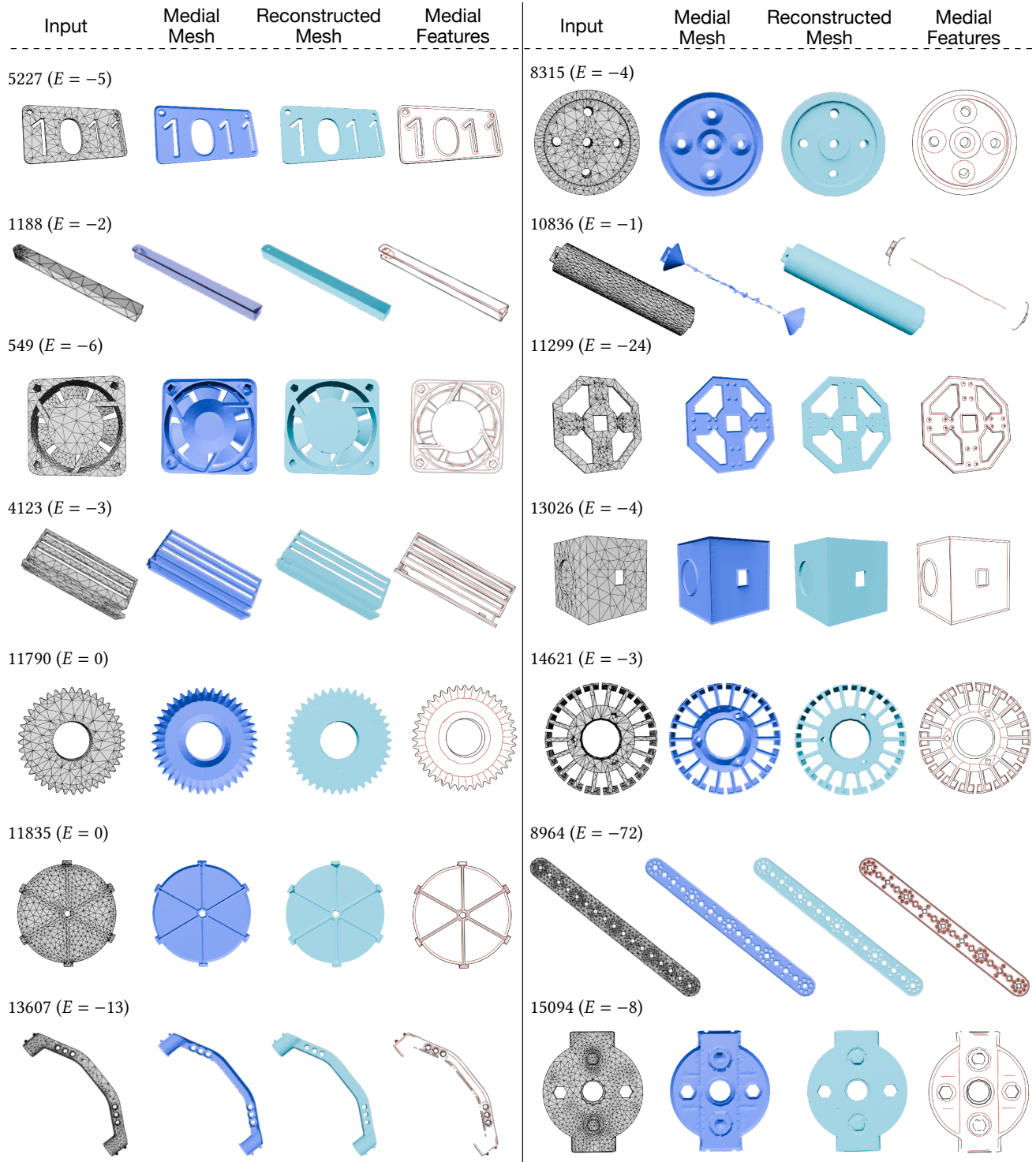


Fig. 12. Visualization of models shown in Table 1. From left to right are the input tetrahedral meshes, the generated medial meshes, the surfaces reconstructed from our medial meshes, and the extracted medial features. For the medial features, the black curves are the external features and the red curves are the internal features.